

## Optimal slicing of free-form surfaces

Tait S. Smith<sup>a</sup>, Rida T. Farouki<sup>a,\*</sup>, Mohammad al-Kandari<sup>a</sup>,  
Helmut Pottmann<sup>b</sup>

<sup>a</sup> *Department of Mechanical and Aeronautical Engineering,  
University of California, Davis, CA 95616, USA*

<sup>b</sup> *Institut für Geometrie, Technische Universität Wien, Wiedner Hauptstrasse 8-10, A-1040 Wien, Austria*

Received March 2001; revised August 2001

---

### Abstract

Many applications, such as contour machining, rapid prototyping, and reverse engineering by laser scanner or coordinate measuring machine, involve sampling of free-form surfaces along section cuts by a family of parallel planes with equidistant spacing  $\Delta$  and common normal  $\mathbf{N}$ . To ensure that such planar sections provide faithful descriptions of the shape of a surface, it is desirable to choose the relative orientation that maximizes, over the entire surface, the minimum angle between  $\mathbf{N}$  and the local surface normal  $\mathbf{n}$ . We address this optimization problem by computing the (symmetrized) Gauss map for the surface, projecting it stereographically onto a plane, and invoking the medial axis transform for the complement of its image to identify the orientation  $\mathbf{N}$  that is “most distant” from the symmetrized Gauss map boundary. Using a Gauss map algorithm described elsewhere, the method is implemented in the context of bicubic Bézier surfaces, and applied to the problem of minimizing the greatest scallop height incurred in contour machining of surfaces using a 3-axis milling machine with a ball-end cutter. © 2001 Elsevier Science B.V. All rights reserved.

*Keywords:* Free-form surface; Planar slicing; Surface normal; Gauss map; Stereographic projection; Medial axis transform; Contour machining; Scallop height

---

### 1. Introduction

A common approach to path planning for free-form surface manufacturing and inspection applications is based on *contouring*—i.e., the computation of a family of sections of the surface by a set of equidistant parallel planes. It is common knowledge,

---

\* Corresponding author.

*E-mail addresses:* tsmith@ucdavis.edu (T.S. Smith), farouki@ucdavis.edu (R.T. Farouki), malkand@ucdavis.edu (M. al-Kandari), pottmann@geometrie.tuwien.ac.at (H. Pottmann).

from topographical maps, that such “surface contours” become widely-spaced and give a poor indication of surface shape at points where the surface tangent plane is parallel to the sectioning planes. In many applications, the orientation of the sectioning planes relative to the surface is a free parameter, that can be specified *a priori*. Hence, the question arises as to how to identify the “optimal” orientation—that maximizes, over the entire surface, the minimum angle between the normal  $\mathbf{N}$  of the sectioning planes and the local surface normal  $\mathbf{n}$  at each point.

A typical context for this problem is the *contour machining* of free-form surfaces, where the tool/surface contact loci correspond to planar sections of the surface (Chen and Ravani, 1987; Farouki et al., 1999). Although one usually imagines sectioning planes at fixed  $z$  heights, parallel planes of *any* orientation may be used in contour machining. In the case of a ball-end mill, the tool sweeps out a sequence of *canal surfaces*, i.e., envelopes of the motion of a sphere along given curves. The union of such canal surfaces yields ridged protrusions called “scallop” between adjacent contact loci on the machined surface, and an optimum path planning strategy must seek to suppress the *scallop height* above the desired surface to within a prescribed tolerance, while maintaining a reasonable overall machining time. This minimizes the need for subsequent grinding or polishing operations, to achieve acceptable accuracy and smoothness of the surface.

Our intent here is to address the problem of optimal slicing orientations, by analyzing the variation of the surface normal vector (i.e., the Gauss map of the surface) and invoking the *medial axis transform* to identify the unit vector that is “as far as possible” from the set of surface normals: using this vector to define the orientation of the sectioning planes, we avoid parallelism with the tangent plane over the entire surface. Our plan is as follows. After reviewing some basic geometrical considerations in Section 2, we address in Section 3 the problem of finding the optimal contouring orientation. This involves (i) computing the symmetrized Gauss map of the surface, and its stereographic projection; (ii) finding the medial axis transform for the complement of the projected Gauss map; and (iii) optimizing a combination of the radius function and position along the medial axis edges. In Section 4 the method is applied to contour machining of surfaces with a ball-end mill: results for contour paths of optimal and non-optimal orientation (and nearly equal overall lengths) are compared. Finally, in Section 5 we make some concluding remarks about the practical use of the optimal surface slicing scheme, and its possible extensions.

## 2. Planar slicing of surfaces

We focus in this paper on sectioning a single tensor-product bicubic surface<sup>1</sup> patch, specified (Farin, 1993) in the Bernstein–Bézier form

$$\mathbf{r}(u, v) = \sum_{j=0}^3 \sum_{k=0}^3 \mathbf{p}_{jk} b_j^3(u) b_k^3(v), \quad (u, v) \in [0, 1] \times [0, 1], \quad (1)$$

<sup>1</sup>The procedure can be easily extended to triangular patches, B-spline surfaces, etc.

by a  $4 \times 4$  array of control points  $\mathbf{p}_{jk}$ . Here the cubic Bernstein basis functions on  $[0, 1]$  are defined by

$$b_i^3(t) = \binom{3}{i} (1-t)^{3-i} t^i, \quad i = 0, \dots, 3.$$

The surface (1) is assumed to be regular—i.e.,  $\mathbf{r}_u \times \mathbf{r}_v \neq \mathbf{0}$  everywhere, and hence the unit normal vector is defined at each point by

$$\mathbf{n}(u, v) = \frac{\mathbf{r}_u \times \mathbf{r}_v}{|\mathbf{r}_u \times \mathbf{r}_v|}. \quad (2)$$

Let  $\mathbf{r} = (x, y, z)$  be a free point in space,  $\mathbf{N} = (N_x, N_y, N_z)$  be a given unit vector, and  $\Delta$  be a given distance. Then, for integer  $k$  values, the equations

$$\mathbf{N} \cdot \mathbf{r} = k\Delta \quad (3)$$

define a set of parallel planes with equidistant spacing  $\Delta$  and common normal  $\mathbf{N}$  (the quantity  $k\Delta$  is the distance of the  $k$ th plane from the origin). Consider the sections of the surface (1) by the family of planes (3). On the  $k$ th section curve, the surface has a normal  $\mathbf{n}$  that, in general, varies with position along this curve. At each point the surface normal  $\mathbf{n}$  is typically distinct<sup>2</sup> from the normal  $\mathbf{N}$  of the planes, and if  $\Delta$  is small compared to the magnitudes of the surface principal curvatures at that point, the quantity

$$\ell \approx \frac{\Delta}{\sqrt{1 - (\mathbf{N} \cdot \mathbf{n})^2}} \quad (4)$$

gives an approximate measure of the distance between the  $k$ th and  $(k+1)$ th section curves, in the plane spanned by  $\mathbf{N}$  and  $\mathbf{n}$ . We may illustrate this with a sphere of radius  $R$ , sectioned by equidistant planes parallel to the equator. At the equator, the spacing between section curves is  $\ell \approx \Delta$  because  $\mathbf{N}$  and  $\mathbf{n}$  are orthogonal, but  $\ell$  increases monotonically without bound as we approach the north pole and  $\mathbf{n}$  becomes more nearly parallel with  $\mathbf{N}$ .

When contour machining a surface with a spherical tool, the quantity  $\ell$ —the (variable) “step-over” between toolpaths—is a key influence on the quality of the machined surface, since (for a fixed tool radius  $r$ ) it determines the local scallop height. In the trivial case of a plane surface machined using linear paths with equidistant spacing  $\ell$  ( $< 2r$ ), the scallop height is (Choi and Gerard, 1998; Marciniak, 1991):

$$h = r - \sqrt{r^2 - \left(\frac{1}{2}\ell\right)^2} \quad \left(\approx \frac{\ell^2}{8r} \text{ if } \ell \ll 2r\right).$$

For a general free-form surface,  $h$  is a very complicated function of the local surface geometry, instantaneous tool-path direction on the surface, etc., that does not admit a simple closed-form expression.<sup>3</sup> Nevertheless, it is obvious that  $h$  will always be a monotone-increasing function of  $\ell$ . Hence, for a given surface, tool radius  $r$ , and contour spacing  $\Delta$ , we can minimize the greatest scallop height over the machined surface by choosing an orientation  $\mathbf{N}$  for the sectioning planes that is “as far as possible” from parallelism with the normal  $\mathbf{n}$  over the entire surface, so as to minimize (4).

<sup>2</sup> In fact, the coincidence of  $\mathbf{n}$  and  $\mathbf{N}$  identifies a *singular point* of the section curve.

<sup>3</sup> See, however, (Kim and Chu, 1994) for the case of cylindrical and spherical surfaces.

Finally, we note that to obtain tool/surface contact loci corresponding to surface contours on equidistant planes, the center of the spherical tool must follow appropriate paths on the *offset surface* (Farouki, 1986). The contouring algorithm of (Farouki et al., 1999) is employed here—this directly generates sets of point/tangent data on the offset tool paths, suitable for adaptive fitting with quintic PH space curves that ensures a prescribed accuracy for the tool paths. The PH quintic tool path descriptions are passed directly to the real-time CNC interpolator of an open-architecture 3-axis mill, capable of executing both constant and variable feedrates. We refer the reader to (Farouki et al., 1999) for complete details.

### 3. Optimal slicing orientation

Although conceptually quite simple, the task of identifying the optimal slicing orientation  $\mathbf{N}$  for any given surface is a computationally challenging task. We partition this task into three phases—(i) computation of the (symmetrized) Gauss map; (ii) construction of the medial axis transform for the complement of the symmetrized Gauss map, after stereographic projection to the plane; and (iii) optimization of a function of radius and position along edges of the medial axis. Since (i) has already been addressed in detail (Smith and Farouki, 2001), we discuss it only briefly in Section 3.1, and concentrate on (ii) and (iii) in Sections 3.2–3.4.

#### 3.1. Computing the Gauss map

The *Gauss map* or “spherical image” (do Carmo, 1976; Hilbert and Cohn-Vossen, 1952) of the surface (1) associates, with each point on it, the point of the unit sphere  $\mathcal{S}$  indicated by the normal (2). In general, the Gauss map occupies some area  $\Omega \subseteq \mathcal{S}$ , but the correspondence between points of  $\mathbf{r}(u, v)$  and of  $\Omega$  is not necessarily one-to-one, since distinct surface points may exhibit identical normals. For the purpose of determining optimal contouring orientations, we do not distinguish between a normal  $\mathbf{n}$  and its negation  $-\mathbf{n}$ . We are thus concerned with the “symmetrized” Gauss map, i.e., for each normal  $\mathbf{n}$  of the oriented surface (1), the antipodal point  $-\mathbf{n}$  on  $\mathcal{S}$  also belongs to the symmetrized Gauss map.

The boundary  $\partial\Omega$  of the Gauss map comprises, in general, a set of curve segments on  $\mathcal{S}$  corresponding to the variation of  $\mathbf{n}$  along the boundary of the patch (1) and along its *parabolic lines* (loci of vanishing Gaussian curvature). A systematic approach to computing a polygonal approximation of  $\partial\Omega$ , which can be refined to any specified accuracy, has been described elsewhere (Smith and Farouki, 2001). The parabolic lines are computed by identifying points of vanishing Gaussian curvature with the zero-set of a bivariate polynomial in Bernstein form: this zero-set can then be isolated using subdivision and the variation-diminishing property to govern a quadtree decomposition of the surface parameter domain  $(u, v) \in [0, 1] \times [0, 1]$ . Once the images of the patch boundaries and parabolic lines on the unit sphere  $\mathcal{S}$  are determined, a standard boundary-extraction scheme may be invoked to select the set of oriented subsegments defining  $\partial\Omega$ . The reader may refer to (Smith and Farouki, 2001) for complete details.

In contouring a surface, we wish to avoid parallelism of the normal  $\mathbf{N}$  to the section planes with the surface normal  $\mathbf{n}$ . Thus, suitable instances of  $\mathbf{N}$  correspond to points in the *complement*  $\Omega_c = \mathcal{S} - \Omega$  of the (symmetrized) Gauss map. In fact, we shall identify the *optimal* contouring orientation  $\mathbf{N}_*$  with the center of the largest circle inscribed within the region  $\Omega_c$  on  $\mathcal{S}$ . If we take the normal  $\mathbf{n}$  at a particular point of (1) to define the “north pole” of  $\mathcal{S}$ , the complement  $\Omega_c$  of the symmetrized Gauss map typically occupies an annular region on the unit sphere, that does not contain the north and south poles. Our intent is to identify the largest circle that can be inscribed within  $\Omega_c$  by computing the medial axis transform of this region.

### 3.2. Stereographic projection

Since it is easier to perform the medial axis computation in the plane, rather than on the sphere, we begin by making a *stereographic projection* (Brannan et al., 1999) of the symmetrized Gauss map. Circles are mapped to circles under this projection<sup>4</sup> (provided they do not pass through the north pole), but they do not preserve ordering by radii. Thus, we cannot simply “read off” the largest circle in  $\Omega_c$  from the medial axis transform of its planar image. Instead, we must optimize a more involved function of radius *and* distance from the origin over the edges of the planar medial axis, in order to identify this largest circle.

Imagine the unit sphere  $\mathcal{S}$  with center at the origin  $(0, 0, 0)$  of a Euclidean space  $(x, y, z)$ , and a family of rays emanating from its “north pole” at  $(0, 0, 1)$  through each point of  $\mathcal{S}$ . The intersections of these rays with the  $(x, y)$  plane define a one-to-one correspondence between points of the sphere and of the plane. One can verify that, under this map, the point on  $\mathcal{S}$  identified by the unit vector  $\mathbf{n} = (n_x, n_y, n_z)$  has the image point

$$\mathbf{p} = (x, y) = \left( \frac{n_x}{1 - n_z}, \frac{n_y}{1 - n_z} \right) \quad (5)$$

in the plane. Under stereographic projection, the equatorial circle on  $\mathcal{S}$  maps into itself, while the images of the northern and southern hemispheres of  $\mathcal{S}$  occupy the exterior and interior of this circle. The inversion of (5), i.e., the unit normal  $\mathbf{n}$  corresponding to a point  $\mathbf{p} = (x, y)$  in the plane, is

$$\mathbf{n} = (n_x, n_y, n_z) = \left( \frac{2x}{x^2 + y^2 + 1}, \frac{2y}{x^2 + y^2 + 1}, \frac{x^2 + y^2 - 1}{x^2 + y^2 + 1} \right). \quad (6)$$

The stereographic projection of a symmetrized Gauss map has a special structure: for each normal  $\mathbf{n}$ , the antipodal normal  $-\mathbf{n}$  has image point

$$\mathbf{p}' = (x', y') = \left( \frac{-n_x}{1 + n_z}, \frac{-n_y}{1 + n_z} \right), \quad (7)$$

and if we interpret (5) and (7) as complex values  $\mathbf{p} = x + iy$  and  $\mathbf{p}' = x' + iy'$ , they satisfy

$$\bar{\mathbf{p}}\mathbf{p}' = -1.$$

<sup>4</sup> In particular, *maximal* circles in  $\Omega_c$  (touching the boundary  $\partial\Omega_c$  in at least two points) are mapped to maximal circles for the planar image of  $\Omega_c$  under stereographic projection.

This identifies  $\mathbf{p}'$  as the image of  $\mathbf{p}$  under an (elliptic) inversion in the unit circle—i.e.,  $\mathbf{p}'$  and  $\mathbf{p}$  lie on (opposite sides of) a line through the origin, and the product of their distances from the origin is unity (Needham, 1997; Schwerdtfeger, 1979). Thus, to compute the stereographic projection of a symmetrized Gauss map, it suffices to consider only the northern or southern hemisphere of  $\mathcal{S}$ , the image of the other hemisphere being obtained by inversion in the unit circle.

Now under stereographic projection, a circle  $\mathcal{C}$  on the unit sphere  $\mathcal{S}$  maps to a circle  $\tilde{\mathcal{C}}$  on the plane. However, the center of  $\tilde{\mathcal{C}}$  is not merely the image of the center  $\mathcal{C}$  under the map (5), and the radius of  $\tilde{\mathcal{C}}$  depends on both the radius *and* the center of  $\mathcal{C}$ . We may clarify these relations as follows.

If the circle  $\mathcal{C}$  on  $\mathcal{S}$  has center specified by the unit vector  $\mathbf{c} = (c_x, c_y, c_z)$  and (angular) radius  $\alpha$ , its equation in free coordinates  $\mathbf{n} = (n_x, n_y, n_z)$  can be expressed as

$$\mathbf{c} \cdot \mathbf{n} = c_x n_x + c_y n_y + c_z n_z = \cos \alpha. \quad (8)$$

Now the pairs  $(\mathbf{c}, \alpha)$  and  $(-\mathbf{c}, \pi - \alpha)$  evidently specify the *same* circle on  $\mathcal{S}$ . To avoid this ambiguity, we shall require that  $0 \leq \alpha \leq \pi/2$ —the extremes  $\alpha = 0$  and  $\alpha = \pi/2$  then correspond to point circles and great circles on  $\mathcal{S}$ , while all intermediate values define small circles.

We wish to find the center and radius of the planar image  $\tilde{\mathcal{C}}$  of (8) under stereographic projection. Substituting from (6) into (8), re-arranging terms, and using  $c_x^2 + c_y^2 + c_z^2 = 1$ , we obtain

$$\left[ x - \frac{c_x}{\cos \alpha - c_z} \right]^2 + \left[ y - \frac{c_y}{\cos \alpha - c_z} \right]^2 = \left[ \frac{\sin \alpha}{\cos \alpha - c_z} \right]^2$$

as the equation of the image circle  $\tilde{\mathcal{C}}$  in the plane. The center and radius of this circle are given by

$$\mathbf{c}_0 = (x_0, y_0) = \left( \frac{c_x}{\cos \alpha - c_z}, \frac{c_y}{\cos \alpha - c_z} \right) \quad (9)$$

and

$$R = \left| \frac{\sin \alpha}{\cos \alpha - c_z} \right|. \quad (10)$$

We observe that the center  $\mathbf{c}_0$  differs from the image

$$\tilde{\mathbf{c}} = \left( \frac{c_x}{1 - c_z}, \frac{c_y}{1 - c_z} \right)$$

of  $\mathbf{c}$  under (5) by replacement of 1 with  $\cos \alpha$  in the denominator. As  $\alpha \rightarrow 0$ , we see that  $\mathbf{c}_0 \rightarrow \tilde{\mathbf{c}}$  and  $R \rightarrow \alpha |1 - c_z|^{-1}$ . Note also that  $R$  becomes infinite if  $c_z = \cos \alpha$ —under stereographic projection, the image of a circle passing through the north pole of  $\mathcal{S}$  is a line rather than a circle.

We can interpret Eq. (9) geometrically as follows. Consider the right circular cone that is tangent to the unit sphere  $\mathcal{S}$  along the circle  $\mathcal{C}$ . Then if  $\mathbf{v} = (v_x, v_y, v_z)$  is the vertex of this cone, the center (9) of the image circle  $\tilde{\mathcal{C}}$  under stereographic projection is the point at which a line passing through the north pole and the cone vertex  $\mathbf{v}$  intersects the  $(x, y)$  plane.

Consider now a circle  $\tilde{\mathcal{C}}$  in the plane, with radius  $R$  and center at distance

$$\rho = \sqrt{x_0^2 + y_0^2}$$

from the origin. We wish to determine, as functions of  $R$  and  $\rho$ , the radius  $\alpha$  and center  $\mathbf{c} = (c_x, c_y, c_z)$  of the circle  $\mathcal{C}$  on  $\mathcal{S}$  that is mapped to  $\tilde{\mathcal{C}}$  under stereographic projection. To accomplish this, we first note from (5) that the point<sup>5</sup>  $\mathbf{c} = (\sin\theta, 0, \cos\theta)$  on  $\mathcal{S}$  maps to  $\mathbf{p} = (x, 0)$  in the plane, where

$$x = \frac{\sin\theta}{1 - \cos\theta} = \cot \frac{1}{2}\theta.$$

Without loss of generality, we assume that the center of  $\tilde{\mathcal{C}}$  lies on the positive  $x$ -axis, such that  $(x_0, y_0) = (\rho, 0)$ . The diametral points  $(x_1, 0) = (\rho - R, 0)$  and  $(x_2, 0) = (\rho + R, 0)$  then arise from the stereographic projection of points  $\mathbf{c}_1 = (\sin\theta_1, 0, \cos\theta_1)$  and  $\mathbf{c}_2 = (\sin\theta_2, 0, \cos\theta_2)$  on  $\mathcal{S}$ , where

$$\theta_1 = 2 \tan^{-1} \frac{1}{\rho - R} \quad \text{and} \quad \theta_2 = 2 \tan^{-1} \frac{1}{\rho + R}. \quad (11)$$

Since  $\mathbf{c}_1, \mathbf{c}_2$  are diametral points (on a longitudinal circle of  $\mathcal{S}$ ) of the circle  $\mathcal{C}$  that projects to  $\tilde{\mathcal{C}}$ , the radius  $\alpha$  and center  $\mathbf{c} = (\sin\theta, 0, \cos\theta)$  of this circle are evidently given by

$$\alpha = \frac{1}{2}(\theta_1 - \theta_2) \quad \text{and} \quad \theta = \frac{1}{2}(\theta_1 + \theta_2).$$

Substituting from (11) and simplifying, we obtain

$$\alpha = \tan^{-1} \frac{2R}{\rho^2 - R^2 + 1} \quad \text{and} \quad \theta = \tan^{-1} \frac{2\rho}{\rho^2 - R^2 - 1}. \quad (12)$$

In deriving (12) we have implicitly assumed that  $0 < R < \rho < \infty$ , and hence  $0 < \theta_2 < \theta_1 < \pi$ , which yields  $0 < \alpha < \pi/2$ . This assumption is justified by the fact that we are concerned only with circles  $\mathcal{C}$  that lie in the complement  $\Omega_c = \mathcal{S} - \Omega$  of the symmetrized Gauss map. Since, by construction, the north and south poles of  $\mathcal{S}$  do not lie in  $\Omega_c$ , and since the origin is the image of the south pole under stereographic projection, no circle  $\mathcal{C}$  inside  $\Omega_c$  has a planar image  $\tilde{\mathcal{C}}$  that contains the origin—i.e., we must have  $\rho > R$ .

### 3.3. Medial axis transform

The *medial axis* of a planar domain is the locus of centers of maximal circles (touching the boundary in at least two points) that can be inscribed within the domain—it provides an abstraction for the “shape” of the domain. The medial axis transform (MAT) is defined by superposing a radius function on the medial axis, specifying the size of the maximal circles centered on it. The domain boundary can, in principle, be precisely re-constructed from its MAT. The basic properties of MATs and algorithms for their construction have

<sup>5</sup> Here  $\theta$  denotes co-latitude on  $\mathcal{S}$ —i.e., the angular distance from the north pole.

been described by a number of authors: see, for example, (Choi et al., 1997a, 1997b; Lee, 1982; Ramamurthy and Farouki, 1999a, 1999b; Sherbrooke et al., 1996).

We wish to compute the MAT for the complement  $\Omega_c$  of the symmetrized Gauss map, after stereographic projection to the plane. Standard algorithms, described in the cited references, can be invoked to accomplish this. However, a basic problem arises with this approach. The boundary  $\partial\Omega_c$ , being defined by the variation of the normal  $\mathbf{n}$  along patch boundaries and parabolic lines, cannot be represented exactly—and the medial axis changes *qualitatively* if we replace the precise domain boundary by an approximation. When we use a polygonal approximation of the domain boundary, for example, the medial axis exhibits an edge terminating at each convex vertex of the polygon; these edges are absent from the medial axis of the *exact* domain.

Such extraneous medial axis edges, incurred by polygonal approximation of the domain boundary, do not compromise our ability to (approximately) identify the largest circle in  $\Omega_c$ , but they do incur a severe penalty in terms of the cost (and robustness) of the MAT computation as we refine the polygonal approximation<sup>6</sup> to more accurately represent  $\partial\Omega_c$ . The practical consequence of these considerations is that, although the Gauss map algorithm (Smith and Farouki, 2001) can in principle furnish polygonal approximations of any desired accuracy, we must choose “reasonable” tolerances in practice—incurring hundreds rather than thousands of segments in the approximation for  $\partial\Omega_c$ . Although this limits the resolution with which the optimal direction is identified, for most applications very high accuracy in the determination of  $\mathbf{N}_*$  is not warranted.

### 3.4. Identifying the optimal orientation

The optimal contour orientation  $\mathbf{N}_*$  corresponds to the center of the largest maximal circle that fits inside the complement  $\Omega_c$  of the symmetrized Gauss map on the unit sphere  $\mathcal{S}$ . Since we are using a stereographic projection of the symmetrized Gauss map onto the plane, which does not preserve ordering relations among the radii of circles, particular care must be exercised in the process of identifying the largest inscribed circle.

Specifically, we must use expression (12) giving the radius  $\alpha$  of a circle on the sphere in terms of the radius  $R$  and distance  $\rho$  from the origin of its image under stereographic projection to the plane. Suppose we have computed the medial axis transform for the stereographic projection of the complement of the symmetrized Gauss map: each element is described parametrically in the form  $(x(t), y(t), R(t))$  for  $t \in [0, 1]$ , the coordinates  $(x(t), y(t))$  describing a locus of centers of maximal disks, and the function  $R(t)$  specifying the radii of these maximal disks. We write

$$\rho(t) = \sqrt{x^2(t) + y^2(t)}$$

for the radial distance of a medial axis point from the origin. Since, in general, both  $R$  and  $\rho$  vary along edges of the medial axis of the planar projection of  $\Omega_c$ , we must seek

<sup>6</sup> It may be thought that this problem can be circumvented by using  $C^2$  piecewise-cubic (in lieu of polygonal) approximations to the segments of  $\partial\Omega_c$ . For domains with (piecewise) smooth curved boundaries, however, the MAT computation becomes much more difficult—and there is still no guarantee of topological fidelity to the exact medial axis.

extrema of  $\alpha$  at both the endpoints and along the interior of such edges. Interior extrema can be identified from the condition

$$\frac{d}{dt} \tan \alpha = \frac{d}{dt} \frac{2R}{\rho^2 - R^2 + 1} = 0,$$

which leads to the problem of finding roots  $t \in (0, 1)$  of the equation

$$[x^2(t) + y^2(t) + R^2(t) + 1]R'(t) - 2[x(t)x'(t) + y(t)y'(t)]R(t) = 0. \quad (13)$$

The values of  $\tan \alpha$  at  $t = 0$  and  $t = 1$  and at each interior extremum must be compared, to find the largest. Suppose, on repeating this process for each element of the medial axis transform, we find that the greatest value of  $\tan \alpha$  corresponds to a circle in the plane with center  $(x_*, y_*)$  and radius  $R_*$ . Then, writing  $\rho_*^2 = x_*^2 + y_*^2$  and using the results of Section 3.2, the optimal contouring orientation can be determined as

$$\mathbf{N}_* = \frac{(2x_*, 2y_*, \rho_*^2 - R_*^2 - 1)}{\sqrt{4\rho_*^2 + (\rho_*^2 - R_*^2 - 1)^2}}. \quad (14)$$

We can also interpret Eq. (13) geometrically, as follows. The medial axis of the spherical domain  $\Omega_c$  can be regarded as the central projection of a spatial curve  $\mathbf{v}(t)$  onto the sphere  $\mathcal{S}$ , with center of projection at the north pole  $(0, 0, 1)$ . The curve  $\mathbf{v}(t)$  comprises the vertices of the set of right circular cones circumscribed to the maximal circles of  $\Omega_c$  (see Section 3.2 above). Moreover, a maximum radius of such circles corresponds to a maximum distance of  $\mathbf{v}(t)$  from the center  $(0, 0, 0)$  of  $\mathcal{S}$ , which implies orthogonality of  $\mathbf{v}(t)$  and its first derivative  $\dot{\mathbf{v}}(t)$ —this condition gives rise to Eq. (13).

Now the medial axis of a polygonal domain comprises both linear (line/line or point/point bisector) and parabolic (point/line bisector) segments, which may be described in Bézier form,

$$\mathbf{r}(t) = (x(t), y(t)) = \sum_{k=0}^n \mathbf{p}_k \binom{n}{k} (1-t)^{n-k} t^k \quad \text{for } t \in [0, 1],$$

with  $n = 1$  in the former case and  $n = 2$  in the latter. Now for the MAT, we must specify the radius function along each segment. Each case gives rise to a different form for  $R(t)$ . For a segment of a line/line bisector, we have

$$R(t) = [d_0(1-t) + d_1t] \sin \psi, \quad (15)$$

where  $d_0, d_1$  are the distances of the end-points  $\mathbf{p}_0, \mathbf{p}_1$  of the bisector segment from the point of intersection of the two lines, and  $2\psi$  is the angle between them (if the two lines are parallel,  $R(t) = \text{constant}$ ). Similarly, for a segment of a point/point bisector, equidistant from points  $\mathbf{a}$  and  $\mathbf{b}$ , we have

$$R(t) = \sqrt{[d_0(1-t) + d_1t]^2 + h^2}, \quad (16)$$

where  $d_0, d_1$  are the distances of the end-points  $\mathbf{p}_0, \mathbf{p}_1$  of the bisector segment from the mid-point  $\mathbf{c} = \frac{1}{2}(\mathbf{a} + \mathbf{b})$ , and  $2h = |\mathbf{a} - \mathbf{b}|$ . Finally, for the case of a parabolic point/line bisector segment defined by control points  $\mathbf{p}_0, \mathbf{p}_1, \mathbf{p}_2$ , we note first (Piegl and Tiller, 1995) that the focus of the parabola is given by

$$\mathbf{f} = \mathbf{p}_1 + \frac{|\mathbf{p}_1 - \mathbf{p}_0|^2(\mathbf{p}_2 - \mathbf{p}_1) - |\mathbf{p}_2 - \mathbf{p}_1|^2(\mathbf{p}_1 - \mathbf{p}_0)}{|\mathbf{p}_2 - 2\mathbf{p}_1 + \mathbf{p}_0|^2}.$$

The radius function may then be expressed as

$$R(t) = \sqrt{|\mathbf{p}_0(1-t)^2 + \mathbf{p}_1 2(1-t)t + \mathbf{p}_2 t^2 - \mathbf{f}|^2}, \quad (17)$$

which is the square-root of a quartic polynomial in  $t$ .

Upon substituting any of the forms (16), (15), (17) for  $R(t)$  into (13), the latter can be rationalized to yield a *polynomial* equation in  $t$  for the extrema of  $\tan \alpha$ . This polynomial is cubic for (16); quadratic for (15); and of degree 7 for (17). For numerical stability (Farouki and Rajan, 1987, 1988) it is constructed in Bernstein form, and its real roots on  $[0, 1]$  can then be computed by standard methods (Lane and Riesenfeld, 1981).

#### 4. Application to contour machining

The optimal slicing algorithm was tested by using it to generate tool paths for contour machining of free-form surfaces. To illustrate the improvement in surface quality obtained by use of optimal contour orientations, the surfaces were machined with contouring planes defined by both the optimal vector  $\mathbf{N}_*$  and the nominal vector  $\mathbf{N} = (0, 0, 1)$ . We present here results for two bicubic test surfaces—both surfaces have a  $3 \times 3$  inch footprint on the  $(x, y)$  plane, with control points arranged over rectangular  $(x, y)$  grids: the variation of the control-point  $z$  coordinates defines the shape of the surfaces.

Table 1 lists some parameters for these machining experiments. A 3-axis milling machine with a  $\frac{1}{2}$  inch diameter ball-end cutter was used to cut both surfaces. Although use of a toroidal (corner-radius) cutter is often preferred for efficiency, the ball-end mill allows for a simpler path-planning strategy. Similar considerations apply to the scallops incurred by the use of a toroidal cutter, although the analysis for this case—and for the extension to 5-axis machining—becomes much more complicated.

Table 1  
Parameters for surface contour machining experiments

Surface	$\Delta$ (in)	$\mathbf{N}$	Total path length (in)	# connected components
#1 nominal	0.0051	(0.0, 0.0, 1.0)	369.41	211
#1 optimal	0.0250	(0.248, -0.969, 0.001)	369.95	146
#2 nominal	0.0100	(0.0, 0.0, 1.0)	359.51	358
#2 optimal	0.0267	(0.975, -0.221, -0.002)	359.23	134

Using a fixed spacing  $\Delta$  for the sectioning planes, that is independent of their orientation  $\mathbf{N}$ , often leads to large variations in the overall length of the tool paths. Thus, to ensure a fair comparison of the improvement in surface finish obtained with the optimal orientation  $\mathbf{N}_*$  over the nominal orientation  $\mathbf{N} = (0, 0, 1)$ , we adjust  $\Delta$  in these two cases so as to give an (approximately) equal total path length, as seen in Table 1.

#### 4.1. Test surface #1

The first test surface, shown in Fig. 1, is defined by the control points

$$\begin{aligned} \mathbf{p}_{00} &= (0, 0, 0.48), & \mathbf{p}_{01} &= (1, 0, 1.00), & \mathbf{p}_{02} &= (2, 0, 0.80), & \mathbf{p}_{03} &= (3, 0, 0.40), \\ \mathbf{p}_{10} &= (0, 1, 0.90), & \mathbf{p}_{11} &= (1, 1, 1.41), & \mathbf{p}_{12} &= (2, 1, 0.60), & \mathbf{p}_{13} &= (3, 1, 0.60), \\ \mathbf{p}_{20} &= (0, 2, 1.00), & \mathbf{p}_{21} &= (1, 2, 0.88), & \mathbf{p}_{22} &= (2, 2, 0.00), & \mathbf{p}_{23} &= (3, 2, 0.72), \\ \mathbf{p}_{30} &= (0, 3, 0.80), & \mathbf{p}_{31} &= (1, 3, 0.60), & \mathbf{p}_{32} &= (2, 3, 0.40), & \mathbf{p}_{33} &= (3, 3, 0.80). \end{aligned}$$

Contour tool paths corresponding to the non-optimal orientation  $\mathbf{N} = (0, 0, 1)$  and fixed spacing  $\Delta = 0.0051$  inch are shown<sup>7</sup> for this surface in Fig. 2.

The symmetrized Gauss map for test surface #1, with its stereographic projection onto the plane, are illustrated in Fig. 3. The symmetrized Gauss map comprises two small

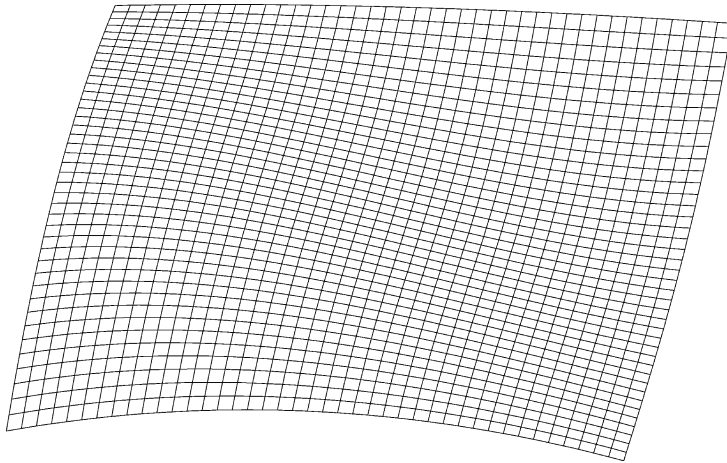


Fig. 1. The bicubic patch used as test surface #1.

<sup>7</sup> For clarity, Fig. 2—and subsequent tool-path plots in Figs. 6, 9, 13—actually show only alternate contouring paths, since these paths are rather densely distributed.

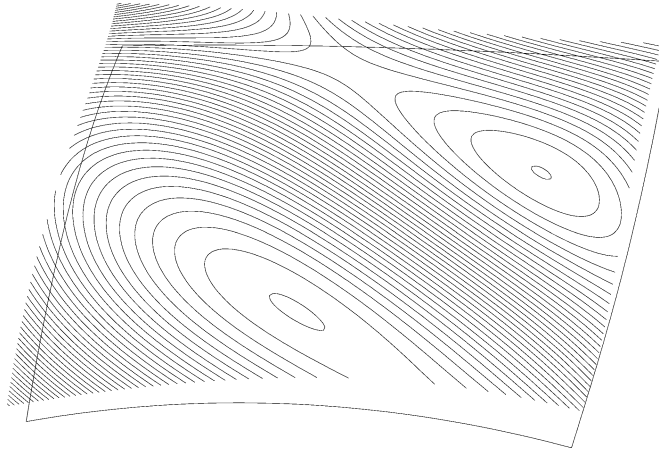


Fig. 2. Tool paths for surface #1, corresponding to contours on  $z$ -planes with common normal  $\mathbf{N} = (0, 0, 1)$  and spacing  $\Delta = 0.0051$  as tool/surface contact loci (the tool paths are spatial curves that lie on the offset surface).

simply-connected “polar caps” on the sphere that encompass the north and south poles. Note that, whereas the south polar cap has a compact image (barely distinguishable in Fig. 3) about the origin, the north polar cap has a highly distended image—for reference, the image of the equator is shown as a dashed circle. The complement of the symmetrized Gauss map is the annular region delineated by the boundaries of the north and south polar caps. We are interested in identifying the inscribed circle of this planar region that maximizes  $\alpha = \tan^{-1} 2R/(\rho^2 - R^2 + 1)$ , where  $R$  is the circle radius and  $\rho$  is the distance of the center from the origin.

Fig. 4 shows the medial axis for the complement of the symmetrized Gauss map, after stereographic projection to the plane. Each linear/parabolic edge of the medial axis is parameterized on the interval  $t \in [0, 1]$  and carries an associated radius function  $R(t)$ . By inspecting every medial axis segment for end-point or interior extrema of  $\tan \alpha$ , as described in Section 3.4, the inscribed circle furnishing the largest  $\alpha$  can be found. This circle is shown in Fig. 4—note that it is *not* simply the largest inscribed circle of the stereographic image. If this circle has center  $(x_*, y_*)$  and radius  $R_*$ , the optimal contour orientation for test surface #1 is found from expression (14) to be

$$\mathbf{N}_* = (0.248, -0.969, 0.001). \quad (18)$$

Fig. 5 illustrates, on the unit sphere, the largest circle that is contained in the complement of the symmetrized Gauss map: its center is defined by  $\mathbf{N}_*$ , and its radius is the largest  $\alpha$  value identified by the above procedure.

Fig. 6 shows tool paths corresponding to the optimal orientation (18) and spacing  $\Delta = 0.025$  inch of the contouring planes, chosen to yield a total length for the tool paths approximately equal to that in the case  $\mathbf{N} = (0, 0, 1)$ . Finally, Fig. 7 shows the surface

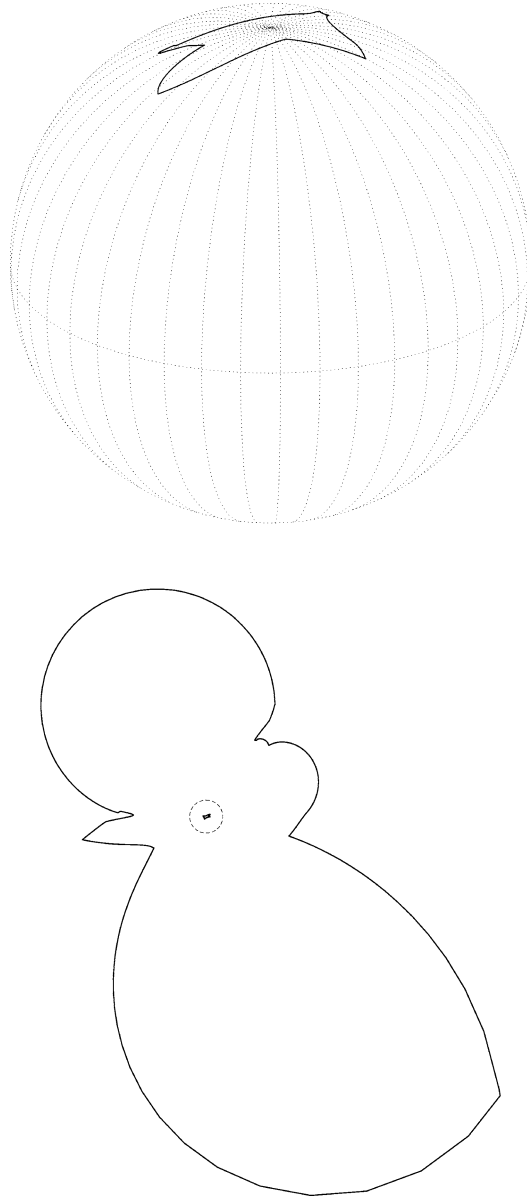


Fig. 3. Upper: symmetrized Gauss map for surface #1; note that the part encompassing the south pole is hidden on the far side of the sphere. Lower: annular region generated by stereographic projection of symmetrized Gauss map onto the plane—the dashed circle indicates the image of the equator.

machined in wax, using a  $\frac{1}{2}$  inch ball-end cutter and the non-optimal and optimal tool paths in Figs. 2 and 6.

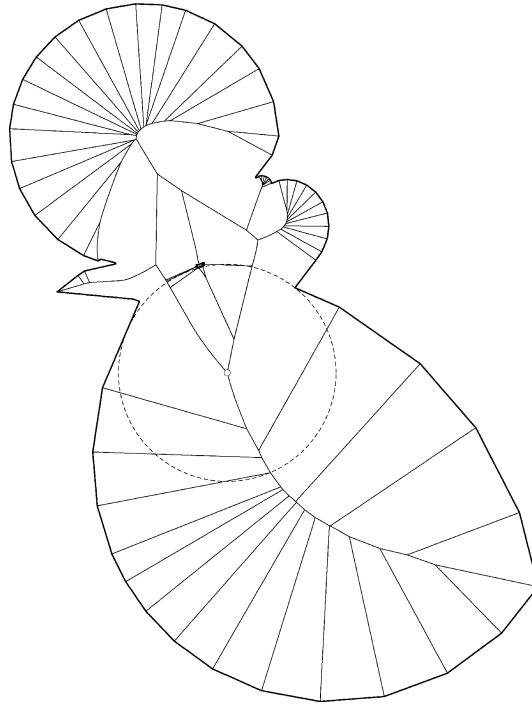


Fig. 4. Medial axis for the complement of the symmetrized Gauss map of test surface #1, after stereographic projection to the plane—note that the polygonal approximation of the boundary incurs a segment of the medial axis terminating at each convex vertex. The inscribed circle that maximizes the angle  $\alpha$  defined by (12) is found by examining all the medial axis segments.

#### 4.2. Test surface #2

Test surface #2, shown in Fig. 8, is defined by the following control points:

$$\begin{aligned}
 \mathbf{p}_{00} &= (0, 0, 1.65), & \mathbf{p}_{01} &= (1, 0, 3.05), & \mathbf{p}_{02} &= (2, 0, 3.05), & \mathbf{p}_{03} &= (3, 0, 2.05), \\
 \mathbf{p}_{10} &= (0, 1, 3.05), & \mathbf{p}_{11} &= (1, 1, 0.00), & \mathbf{p}_{12} &= (2, 1, 4.10), & \mathbf{p}_{13} &= (3, 1, 3.05), \\
 \mathbf{p}_{20} &= (0, 2, 3.05), & \mathbf{p}_{21} &= (1, 2, 4.10), & \mathbf{p}_{22} &= (2, 2, 0.00), & \mathbf{p}_{23} &= (3, 2, 3.05), \\
 \mathbf{p}_{30} &= (0, 3, 2.05), & \mathbf{p}_{31} &= (1, 3, 3.05), & \mathbf{p}_{32} &= (2, 3, 3.05), & \mathbf{p}_{33} &= (3, 3, 1.65).
 \end{aligned}$$

Tool paths for this surface corresponding to constant- $z$  contours with spacing  $\Delta = 0.01$  inch are shown, for a  $\frac{1}{2}$  inch ball-end cutter, in Fig. 9.

Fig. 10 shows the symmetrized Gauss map for test surface #2, together with its stereographic projection onto the plane. This case differs from surface #1, in that surface #2 exhibits much greater variation of the surface normal over its extent, and hence the symmetrized Gauss map occupies a much larger portion of the northern and southern hemispheres (the symmetry properties of surface #2 are also apparent in the Gauss map).

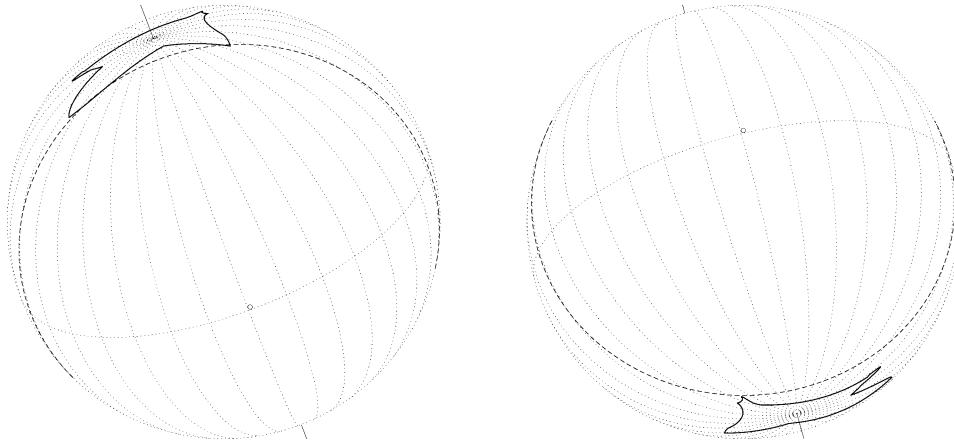


Fig. 5. The maximal inscribed circle in the complement of the symmetrized Gauss map for surface #1, shown on the unit sphere: the center of this circle defines the optimal contouring orientation  $\mathbf{N}_*$ . The two views show how this circle touches the north and south polar caps of the symmetrized Gauss map.

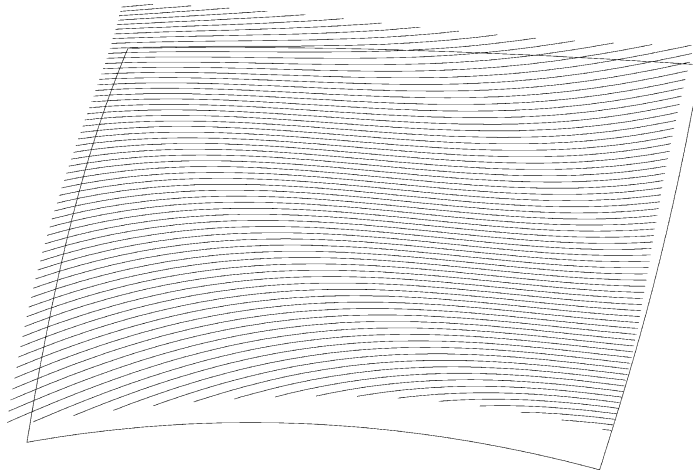


Fig. 6. Tool paths for surface #1, corresponding to contours on planes with the optimal orientation  $\mathbf{N}_*$  given by (18) and fixed spacing  $\Delta = 0.025$ , as the tool/surface contact loci (again, these paths lie on the offset surface).

Thus, under stereographic projection, the boundaries of the northern and southern polar caps are of a more commensurate extent than for surface #1.

The medial axis for the complement of the symmetrized Gauss map, after stereographic projection to the plane, is illustrated in Fig. 11 together with the inscribed circle that

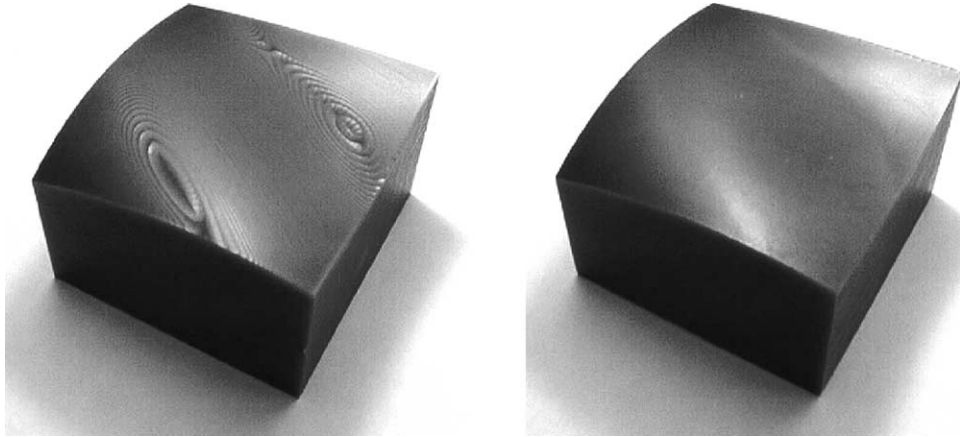


Fig. 7. Test surface #1 machined in wax, using the non-optimal (left) and optimal (right) contouring paths shown in Figs. 2 and 6, respectively, and a  $\frac{1}{2}$  inch ball-end cutter. These tool paths correspond to tool/surface contact loci on parallel planes, and are of approximately equal overall length—a substantial improvement in the surface quality (suppression of scallop height) is apparent when using the optimal orientation rather than  $z$ -contouring.

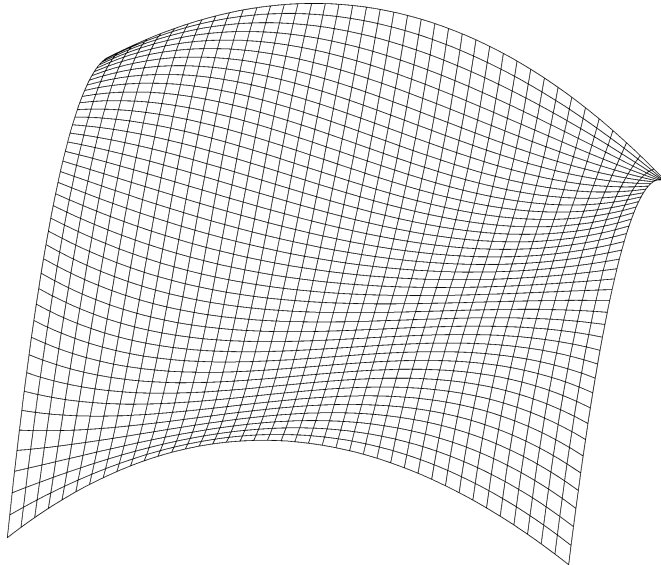


Fig. 8. The bicubic patch used as test surface #2.

identifies the optimal contour orientation. For this surface, the optimal orientation is found to be

$$\mathbf{N}_* = (0.975, -0.221, -0.002). \quad (19)$$

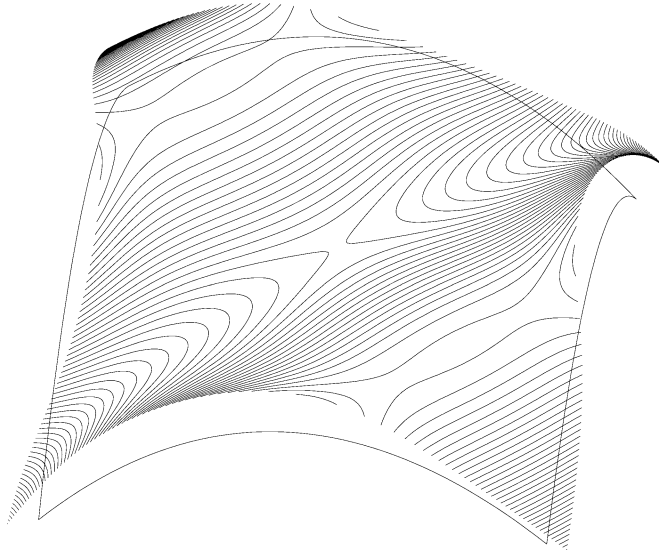


Fig. 9. Tool paths on the offset to surface #2, corresponding to contours on  $z$ -planes with fixed spacing  $\Delta = 0.01$  as the tool/surface contact loci.

In fact, this optimal orientation is not unique, owing to the symmetry of the surface (evident from its control points and the Gauss map). In Fig. 12 we show, on the unit sphere, the maximal circle inscribed in the complement of the symmetrized Gauss map—the center of this circle identifies the optimal contouring orientation (19). The tool paths that correspond to this optimal orientation and a fixed spacing  $\Delta = 0.0267$  inch are illustrated<sup>8</sup> in Fig. 13.

Finally, Fig. 14 shows surface #2, as machined in wax using the non-optimal paths shown in Fig. 9 and the optimal paths shown in Fig. 13. As with surface #1, a significant improvement in surface quality (in terms of the suppression of scallop height) is clearly evident in the machined surfaces.

We observe from Table 1 that, for both surfaces, the number of connected components comprising the tool path (for a given total length) is smaller for the optimal than for the nominal orientation. Thus, in addition to providing an improved surface quality, the optimal orientation is also more efficient in terms of requiring fewer tool retractions and re-positionings.

It should be noted that the optimal orientations (18) and (19) for the two test surfaces are approximate, since they were determined using a polygonal boundary approximation for the stereographic projection of the symmetrized Gauss map. Although the approximation can, in principle, be made as precise as we desire, extremely fine polygonal approximations may tax the robustness of the MAT algorithm (see Section 3.3). Nevertheless, for the application at hand, great accuracy in computing  $\mathbf{N}_*$  is not essential—the examples in Figs. 4 and 11 employ a few hundred polygonal edges to approximate  $\partial\Omega_c$ .

<sup>8</sup> As with surface #1, we display only alternate tool paths in Fig. 13 for clarity.

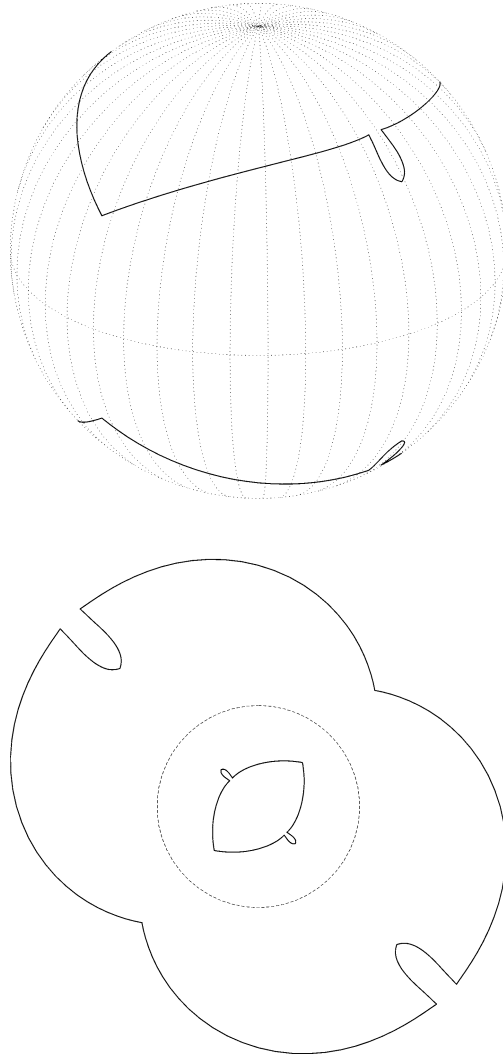


Fig. 10. Upper: the symmetrized Gauss map for surface #2—portions of both the northern and southern polar caps are visible. Lower: stereographic projection onto the plane—the dashed circle is the image of the equator.

The comparison between the “nominal” and “optimal” cases in Figs. 7 and 14 is perhaps a little exaggerated, since  $\mathbf{N} = (0, 0, 1)$  is a poor choice for the former: one can see by inspection that the surface normal  $\mathbf{n}$  coincides with it at certain points. Geometrical intuition may allow one to “guess” a better nominal slicing orientation, although this becomes increasingly difficult for complex surfaces. The algorithm described herein allows the most favorable orientation, in the sense of maximizing the minimum angle between  $\mathbf{N}$  and  $\mathbf{n}$  over the entire surface, to be computed in a deterministic manner.

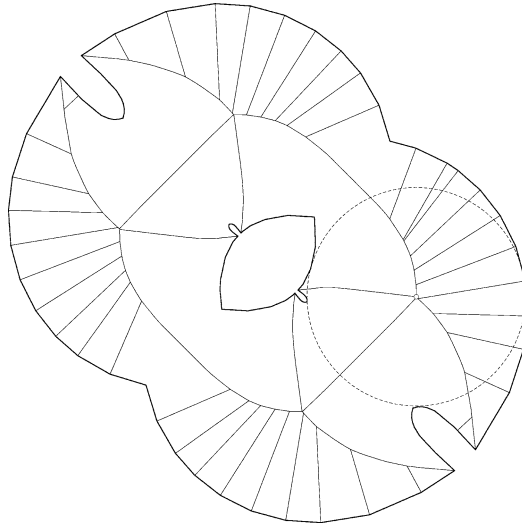


Fig. 11. Medial axis for the complement of the symmetrized Gauss map of test surface #2, after stereographic projection to the plane. The inscribed circle that maximizes the angle  $\alpha$ , defined by expression (12), is also shown.

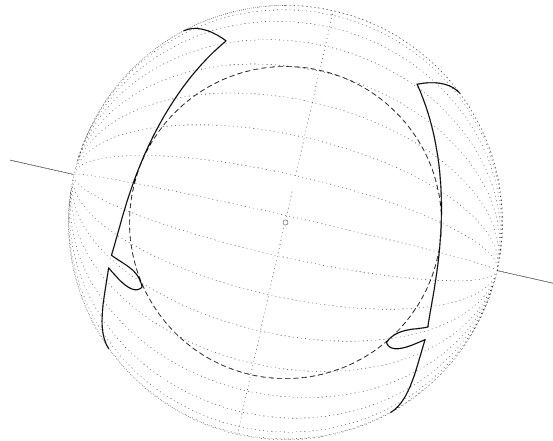


Fig. 12. The largest circle inscribed in the complement of the symmetrized Gauss map for surface #2—its center defines the optimal orientation (19).

## 5. Closure

Our focus in this paper has been on methods to ensure the “quality” of the representation of a surface by a set of contours, corresponding to sections of the surface by a family of equidistant parallel planes. The *optimal* contouring orientation, minimizing the maximum spacing between successive contours, was identified by (i) computing the complement

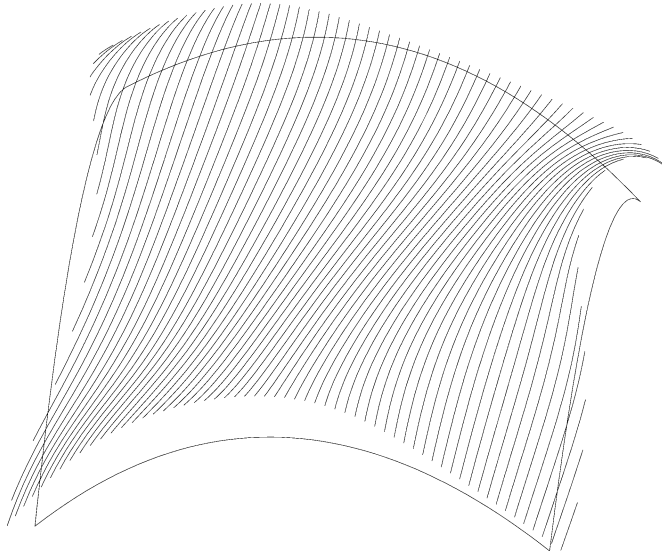


Fig. 13. Tool paths for surface #2, yielding contours on planes with the optimal orientation (19) and spacing  $\Delta = 0.0267$  as tool/surface contact loci.

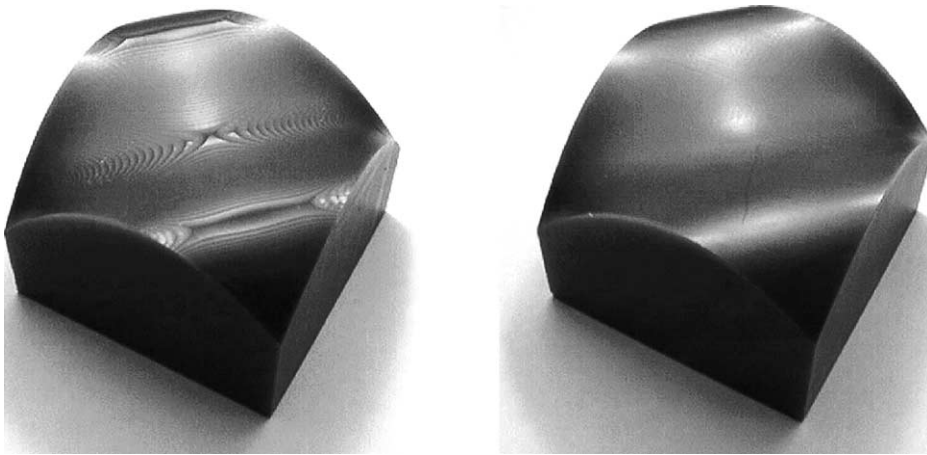


Fig. 14. Comparison of test surface #2 machined in wax, using a  $\frac{1}{2}$  inch ball-end cutter and non-optimal (left) and optimal (right) contouring paths.

of the symmetrized Gauss map; (ii) making a stereographic projection to the plane, and computing the medial axis transform of the image domain; and (iii) maximizing a function of position and radius along the edges of the medial axis.

In the context of contour machining using a ball-end mill, this optimal orientation will ensure that the greatest scallop height over the entire surface is minimized, assuming

that the tool radius  $r$  and the spacing  $\Delta$  remain fixed. Contour machining offers an easy means to ensure full coverage of tool paths over a free-form surface. Since the contour paths depend only on the geometry of the surface, and the orientation and spacing of the sectioning planes, they circumvent potential problems with the surface parameterization. The Gauss map, and the closely-related *visibility map*, have been applied to machining problems before (Chen and Woo, 1992; Elber and Zussman, 1998; Gan et al., 1994; Woo, 1994), but mainly to address accessibility issues rather than the scallop height minimization problem addressed here.

The optimal contour-orientation algorithm described above has potential applications in areas other than NC machining. For example, in rapid prototyping or “layered manufacturing” processes, three-dimensional models are built up by bonding, curing, fusing, or depositing material in layers of finite thickness. The “stepped” nature of the fabricated model surface is especially pronounced in regions where the surface normal is nearly parallel to the build direction, and the use of an optimal contouring orientation can help preclude this circumstance. Similar considerations apply when re-constructing three-dimensional models from planar “slice” data—as obtained, for example, from medical imaging or laser range-finding systems.

## Acknowledgement

This work was supported in part by the National Science Foundation under grant CCR-9902669 and the Austrian Science Fund under grant P13938.

## References

- Brannan, D.A., Esplen, M.F., Gray, J.J., 1999. *Geometry*. Cambridge University Press.
- Chen, Y., Ravani, B., 1987. Offset surface generation and contouring in computer-aided design. *ASME Journal of Mechanisms, Transmissions, and Automation in Design* 109 (1), 133–142.
- Chen, L.-L., Woo, T.C., 1992. Computational geometry on the sphere with application to automated machining. *ASME Journal of Mechanical Design* 114, 288–295.
- Choi, B.K., Gerard, R.B., 1998. *Sculptured Surface Machining: Theory and Applications*. Kluwer Academic, Dordrecht.
- Choi, H.I., Choi, S.W., Moon, H.P., 1997a. Mathematical theory of medial axis transform. *Pacific J. Math.* 181, 57–88.
- Choi, H.I., Choi, S.W., Moon, H.P., Wee, N.S., 1997b. New algorithm for medial axis transform of plane domain. *Graphical Models and Image Processing* 59, 463–483.
- do Carmo, M.P., 1976. *Differential Geometry of Curves and Surfaces*. Prentice-Hall, Englewood Cliffs, NJ.
- Elber, G., Zussman, E., 1998. Cone visibility decomposition of free-form surfaces. *Computer-Aided Design* 30, 315–320.
- Farin, G., 1993. *Curves and Surfaces for Computer Aided Geometric Design*, 3rd edn. Academic Press, Boston.
- Farouki, R.T., 1986. The approximation of non-degenerate offset surfaces. *Computer Aided Geometric Design* 3, 15–43.

- Farouki, R.T., Rajan, V.T., 1987. On the numerical condition of polynomials in Bernstein form. *Computer Aided Geometric Design* 4, 191–216.
- Farouki, R.T., Rajan, V.T., 1988. Algorithms for polynomials in Bernstein form. *Computer Aided Geometric Design* 5, 1–26.
- Farouki, R.T., Tsai, Y.-F., Yuan, G.-F., 1999. Contour machining of free-form surfaces with real-time PH curve interpolators. *Computer Aided Geometric Design* 16, 61–76.
- Gan, J.G., Woo, T.C., Tang, K., 1994. Spherical maps: construction, properties, and approximation. *ASME Journal of Mechanical Design* 116, 357–363.
- Hilbert, D., Cohn-Vossen, S., 1952. *Geometry and the Imagination*. Chelsea, New York.
- Kim, B.H., Chu, C.N., 1994. Effect of cutter mark on surface roughness and scallop height in sculptured surface machining. *Computer-Aided Design* 26, 179–188.
- Lane, J.M., Riesenfeld, R.F., 1981. Bounds on a polynomial. *BIT* 21, 112–117.
- Lee, D.T., 1982. Medial axis transformation of a planar shape. *IEEE Transactions on Pattern Analysis and Machine Intelligence* 4, 363–369.
- Marciniak, K., 1991. *Geometric Modelling for Numerically Controlled Machining*. Oxford University Press, Oxford.
- Needham, T., 1997. *Visual Complex Analysis*. Oxford University Press.
- Piegl, L., Tiller, W., 1995. *The NURBS Book*. Springer, Berlin.
- Ramamurthy, R., Farouki, R.T., 1999a. Voronoi diagram and medial axis algorithm for planar domains with curved boundaries I, Theoretical foundations. *J. Comput. Appl. Math.* 102, 119–141.
- Ramamurthy, R., Farouki, R.T., 1999b. Voronoi diagram and medial axis algorithm for planar domains with curved boundaries II, Detailed algorithm description. *J. Comput. Appl. Math.* 102, 253–277.
- Schwerdtfeger, H., 1979. *Geometry of Complex Numbers*. Dover, New York.
- Sherbrooke, E.C., Patrikalakis, N.M., Wolter, F.-E., 1996. Differential and topological properties of medial axis transforms. *Graphical Models and Image Processing* 58, 574–592.
- Smith, T.S., Farouki, R.T., 2001. Gauss map computation for free-form surfaces. *Computer Aided Geometric Design* 18, 831–850.
- Woo, T.C., 1994. Visibility maps and spherical algorithms. *Computer-Aided Design* 26, 6–16.